The in-situ growth of atomically dispersed Ni species on CeO2 during low-temperature CH4/CO2 reforming

SCHOLARONE™
Manuscripts

ARTICLE

The in-situ growth of atomically dispersed Ni species on CeO$_2$ during low-temperature CH$_4$/CO$_2$ reforming

Hui Wang,*[a] Yansu Hu,[a] Alexander Adogwa,[b] Ming Yang*[b], Tong-Bu Lu*[a]

The ceria-supported nickel catalyst is a widely used benchmark for low-temperature dry reforming of methane (DRM). Nonetheless, whether the atomically dispersed Ni species aggregates during the reaction and which species boost the activity remains elusive. Herein, we designed a group of Ni/CeO$_2$ catalysts ranging from single atoms to nanoparticles (NPs) by carefully increasing the Ni loading from 0.5 to 1.6 wt.%. The actual Ni states were verified by a series of advanced characterizations. Through DRM studies, characterizations of reaction-spent Ni species and carbon deposits, kinetics, and time-resolved in situ infrared spectroscopy, we found that the atomically dispersed Ni species aggregate into clusters or NPs upon contact with the DRM reactants, which is necessary for the DRM activity. These in-situ aggregated Ni species boosted the overall reaction with less carbon formation, while the reaction-spent 0.5Ni/CeO$_2$ still retaining some single atoms produced more graphitic carbon during the reaction.

Introduction

Single-atom catalysts have opened a new dimension in heterogeneous catalysis and have attracted extensive attention since 2011.[1,2] They maximize the utilization of supported metals by shrinking required metals from nanoparticles (NPs) to atomically dispersed atoms on various supports.[3,4] The supported single atoms featuring unique chemical and physical properties are supposed to be highly active and selective for numerous heterogeneous reactions.[5] The excellent reactivity and selectivity have been verified in many oxidative reactions, such as CO oxidation. However, in the presence of reductive reactants at high temperatures, the metal-support bonds used to stabilize the single atoms could break readily, resulting in a mixture of single atoms, clusters, and NPs. This gives rise to the misunderstanding of active sites and reaction mechanisms.

Here, we chose the low-temperature dry reforming of methane (DRM) as the object reaction to identify the active sites from single atoms to NPs. DRM employs the abundant CO$_2$ and CH$_4$ to produce syngas (CO and H$_2$).[6,7] The products with a low H$_2$/CO ratio can be directly used as the raw materials for Fischer-Tropsch synthesis to obtain value-added liquid fuels and energy chemicals.[8,9] This is a cheap and promising route for urgent CO$_2$ emission control. Almost three decades of studies on DRM reaction have identified Ni catalysts as the most promising candidate,[6,7] but the strong endothermicity at high temperatures and severe coke formation impeded its

commercialization. The recently prevalent DRM operation at lower temperatures with ceria-based materials as supports for oxidizing the generated carbon has sparked new prospects.[10]

In recent reports, Kawi and Gates demonstrated the reduction and agglomeration of isolated cationic platinum atoms on ceria during the DRM reaction at 435 °C using operando X-ray absorption (XAS) and infrared spectra.[11] They found that the formation of clusters or NPs is necessary for CH$_4$ decomposition. However, similar studies and discussions on the widely used benchmark Ni/CeO$_2$ catalysts are still lacking. This is because the lower contrast of Ni compared to Ce atoms renders it fade in the aberration-corrected high-angle annular dark-field scanning transmission electron microscopy (HAADF-STEM) images, making it difficult to distinguish atomically dispersed Ni atoms. To date, whether single-atom Ni species exhibits enhanced DRM activity compared to NPs on ceria, or whether they aggregate during the reaction, remains unclear and even sometimes debatable.

Herein, we designed a group of Ni/CeO$_2$ catalysts from single atoms to NPs by changing the Ni loading with strong electronic adsorption method. Although the combination of aberration-corrected HAADF-STEM and XAS cannot distinguish the single-atom Ni species on ceria, diffuse reflectance infrared Fourier-transform spectroscopy using CO as a probe molecule (CO DRIFTS) and H$_2$ temperature programmed reduction (H$_2$ TPR) with elaborate operation provide a clear demonstration of the predominance of atomically dispersed Ni atoms on the as-prepared 0.5Ni/CeO$_2$. Through DRM studies, characterizations of the reaction-spent Ni species and carbon deposits, kinetics, and time-resolved DRIFTS, we found that the atomically dispersed Ni atoms aggregate into NPs upon contact with DRM reactants at 400 °C. These aggregated, exposed Ni NPs, are the active sites for the DRM reaction, rather than the initial single atoms.

[a.] Institute for New Energy Materials and Low Carbon Technologies, School of Materials Science and Engineering, Tianjin University of Technology, Tianjin 300384, China. Email: wanghui2020@email.tjut.edu.cn; lutongbu@tjut.edu.cn

[b.] Department of Chemical and Biomolecular Engineering, Clemson University, Clemson, SC, 29634, USA. Email: myang3@clemson.edu

Results and discussion

Characterizations of as-prepared catalysts

Highly dispersed Ni species

The physical structure of the Ni/CeO_2 catalysts, including BET surface area and pore structure (Fig. S1), did not show any obvious discrepancy despite different Ni loading. Only the cubic fluorite structure of ceria was detected in the XRD patterns (Fig. S2), and the absence of Ni or NiO signal indicates that all the Ni species are highly dispersed and below the detection limit of XRD. XPS measurements were conducted to analyze the chemical valence of Ni species (Fig. S3). Despite the gradually increasing Ni loading, all Ni species present the oxidation state of +2 valence exclusively (Fig. S3a). Further, the categories and content of Ce and O species are almost identical for all as-prepared catalysts (Fig. S3b, S3c), indicating that the characteristics of CeO_2 support are not affected by the content of Ni loading.

The aberration-corrected HAADF-STEM images and EDS mapping provided a more explicit demonstration of the highly dispersed Ni species (Figs. 1, S4, S5). We did not observe obvious NPs from HAADF-STEM images and EDS mapping, even on $1.6Ni/CeO_2$ with the highest Ni loading. Noteworthy, the loaded Ni has a lower Z^2 value (Z = 28) than Ce (Z = 58), making it difficult to observe in STEM images. Fortunately, EDS mapping can recognize the signal of Ni species. Given that the detection limit of EDS mapping is about 2 nm, the absence of NPs in EDS mapping therefore excludes the presence of Ni NPs (> 2 nm) on the as-prepared catalysts.

We next performed XAS measurement on the two representative $0.5Ni/CeO_2$ and $1.6Ni/CeO_2$ catalysts to analyze the chemical valence and coordination environment of Ni species (Figs. 2, S6, Table S1). The x-ray absorption near-edge structure (XANES) results indicate the oxidation state of Ni atoms in both samples (Fig. 2a), aligning well with XPS spectra (Fig. S3). Extended x-ray absorption fine structure (EXAFS) of $0.5Ni/CeO_2$ was not obtained due to its low Ni loading, while the analysis for $1.6Ni/CeO_2$ further confirmed the absence of Ni-Ni contact (Figs. 2b, S6, Table S1). Each Ni atom was surrounded by six oxygen atoms with the Ni-O distance of 2.02 Å,[12] even on $1.6Ni/CeO_2$ catalyst with the highest Ni loading. At the distances
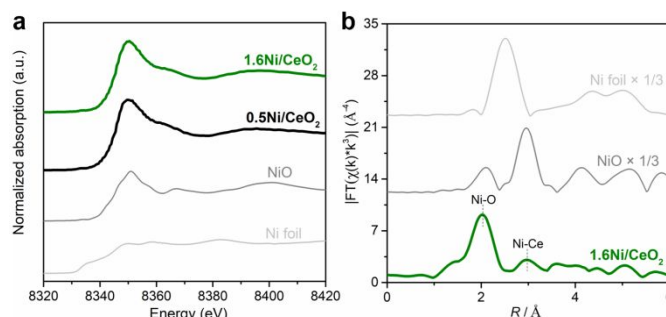

Fig. 2. X-ray absorption spectroscopy (XAS) analyses. (a) Normalized Ni K edge X-ray absorption near-edge structure (XANES) spectra and (b) Fourier transform of extended X-ray absorption fine structure (EXAFS) spectra of Ni K edge (phase corrected).

of 3.03 and 3.13 Å, six Ce atoms are coordinated with the central Ni atom. This demonstrates that most Ni atoms were atomically dispersed or existed in oxidative clusters.[13,14]

Combining the XRD, XPS, HAADF-STEM with EDS mapping, and XAS measurements, we confirmed the high dispersion of Ni species (< 2 nm) in oxidation states for all the as-prepared catalysts when the Ni loading increased from 0.5 to 1.6 wt.%. However, these benchmark characterizations for identifying single-atom catalysts cannot give more elaborate differences in the four catalysts due to the material particularity, i.e., atomically dispersed single atoms, NPs smaller than 2 nm (i.e., clusters), or a mixture.

From single atoms to NPs

CO DRIFTS measurements were meticulously performed on the four as-prepared catalysts to further distinguish the differences in Ni species (Fig. 3). To preserve the original states of Ni species, we only purged the as-prepared catalysts at 500 °C in N_2 to eliminate any possible adsorbed H_2O and CO_2 molecules, without conducting any reduction treatment before CO adsorption. Interestingly, no CO adsorption was observed on $0.5Ni/CeO_2$ (Fig. 3a), but there is a weak vibration at 1918 cm^{-1} on $0.8Ni/CeO_2$ after CO purging (Fig. 3b), attributable to bridged CO adsorption on metallic Ni surface.[15,16] For catalysts with Ni loading of 1.2 and 1.6 wt.%, this vibration peak became stronger and even emerged under the CO atmosphere (Fig. 3c, 3d). We reason that the Ni single atoms predominate on $0.5Ni/CeO_2$, with each Ni atom bonded by O atoms and maintaining a long distance from each other. This decreased the opportunity for aggregation. CO adsorption on these single-atom Ni species is weak and prone to desorb at 30 °C.[17]

Pertaining to $0.8Ni/CeO_2$, some Ni species may exist as oxidative clusters (< 2 nm) and reside close to each other. These small oxidative clusters could be reduced and may further aggregate owing to their proximity to each other. Consequently, CO adsorption on the metallic surface is observed at 1918 cm^{-1} (Fig. 3b). This adsorption becomes more prominent when the Ni loading increases to 1.2 and 1.6 wt.% (Fig. 3c, 3d), indicating a higher surface density of oxidative clusters on the two catalysts.
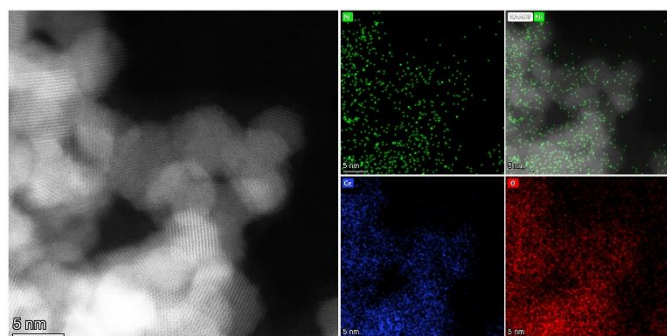

Fig. 1. HAADF-STEM and EDS mapping for the as-prepared $1.6Ni/CeO_2$ sample.
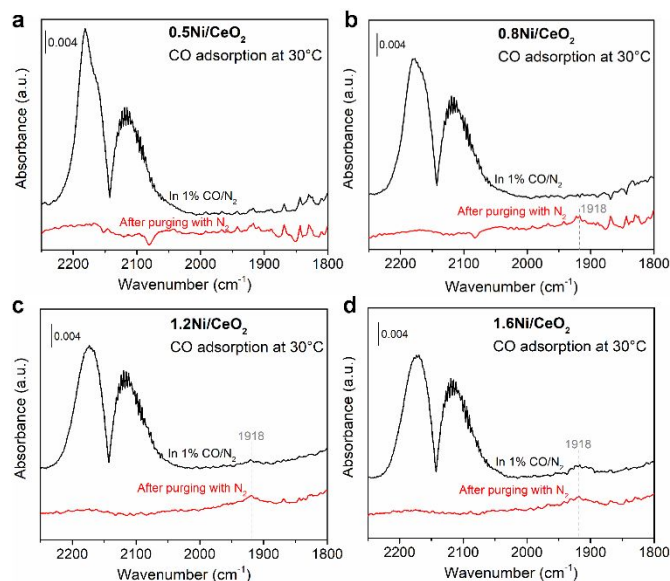
ARTICLE

Fig. 3. CO DRIFTS of as-prepared Ni/CeO_2 samples. The CO adsorption spectra in 1% CO/N_2 and after purging with N_2 for (a) $0.5Ni/CeO_2$, (b) $0.8Ni/CeO_2$, (c) $1.2Ni/CeO_2$, and (d) $1.6Ni/CeO_2$ samples.

Further, we performed H_2 TPR to analyze the specific states of Ni species. As displayed in Fig. 4, there are two reduction peaks at 320 and 490 °C on the Ni-free CeO_2 support, assigning to the reduction of surface and subsurface reactive oxygen,[18,19] respectively. After Ni loading, these reduction peaks shifted to lower temperatures due to the strong interaction between Ni species and ceria. The H_2 consumption below 200 °C can be attributed to the reduction of Ni species and their associated reactive oxygen.[20–23] Specifically, the peaks at 177 and 193 °C on $0.5Ni/CeO_2$ can be assigned to the reduction of Ni single atoms and its associated surface reactive oxygen species, as indicated by the corresponding CO adsorption analysis in Fig. 3. When Ni loading increased to 0.8 wt.%, a lower reduction peak emerged at 148 °C, and it became the exclusive reduction peak on 1.2 and 1.6 wt.% samples. Given the aforementioned characterizations
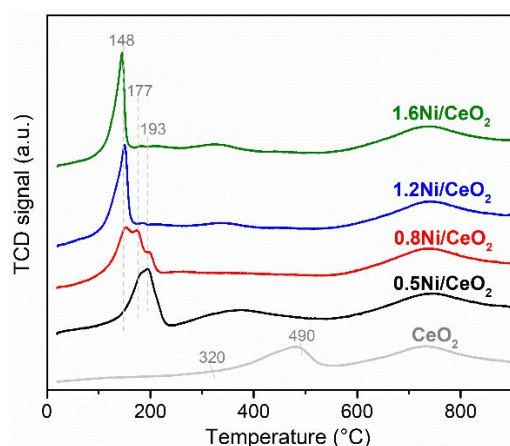

Fig. 4. H_2 TPR curves of ceria and the as-prepared Ni/CeO_2 samples with different Ni loading amount.

and analyses of Ni species, there are only Ni single atoms and oxidative clusters (< 2 nm) on these Ni/CeO_2 catalysts. We therefore assign the reduction peak at 148 °C to the depletion of oxidative nickel clusters and their associated surface reactive oxygen.

Based on the foregoing, the combined CO DRIFTS (Fig. 3) and H_2 TPR (Fig. 4) profiles reveal that Ni single atoms are the predominant species on $0.5Ni/CeO_2$. It becomes a mixture of Ni single atoms and clusters on $0.8Ni/CeO_2$, while Ni clusters (< 2 nm) predominate on $1.2Ni/CeO_2$ and $1.6Ni/CeO_2$ samples.

DRM catalytic activity

We evaluated the DRM reactivity of the four Ni/CeO_2 catalysts from 400 to 500 °C with equimolar CH_4 and CO_2 (Figs. 5, S7). To explore the intrinsic evolution and catalytic performance of the as-prepared Ni species, no pre-reduction was performed before the reaction. When the reaction was run back from 500 °C, the conversions of CH_4 and CO_2 improved dramatically at 450 and 400 °C on $0.5Ni/CeO_2$ (Fig. 5a). This phenomenon also recurred at 400 °C on $0.8Ni/CeO_2$ (Fig. 5b). Nonetheless, the conversions remained basically identical on the $1.2Ni/CeO_2$ and $1.6Ni/CeO_2$ catalysts during the ramping and cooling process (Fig. 5c, 5d). Further, the $1.6Ni/CeO_2$ sample demonstrated good activity stability (Fig. S8). Given the different Ni species on these as-prepared Ni/CeO_2 catalysts, it indicates that the Ni single atoms on $0.5Ni/CeO_2$ and $0.8Ni/CeO_2$ may have aggregated into clusters or NPs during the DRM reaction. These aggregated clusters or NPs, rather than the initial single atoms, boost the overall reaction.

To confirm this speculation, the $0.5Ni/CeO_2$ and $0.8Ni/CeO_2$ catalyst were pre-reduced at 400 °C in 10% H_2 before the reaction (Fig. 5e, 5f) and compared with the scenario without pre-reduction. Intriguingly, the pre-reduced catalysts exhibited better DRM reactivity, demonstrating that the aggregated clusters or NPs are the active sites for DRM reaction. Almost no activity improvement was observed on $0.8Ni/CeO_2$ at 450 °C when running back or with pre-reduction (Fig. 5b, 5f). We reason that this catalyst has a higher surface density of Ni species in single atoms or clusters compared with the $0.5Ni/CeO_2$, and this accelerates the aggregation process during reaction or pre-reduction. More so, we prepared a lower Ni loading sample $0.1Ni/CeO_2$, using the same protocol, which was expected to have more stable and atomically dispersed Ni species compared to the 0.5 wt.% loaded counterpart.[24,25] However, the $0.1Ni/CeO_2$ was inactive for DRM reaction from 400 to 500 °C (Fig. S9), indicating that the aggregation into clusters or NPs is necessary for DRM reaction.

Additionally, the H_2/CO ratio is significantly lower than 1 throughout the entire reaction from 400 to 500 °C (Fig. S7) due to the side reaction of reverse water gas shift,[7,26] which produces CO and H_2O using H_2 and CO_2.[27,28] It is reported that this side reaction prefers to occur on single-atom catalysts, or it would generate methane on NPs.[27] The lowest H_2/CO ratio of $0.5Ni/CeO_2$ among these catalysts suggests that there are still some Ni single atoms present during the reaction. It is difficult to aggregate all the single-atom Ni species with such low
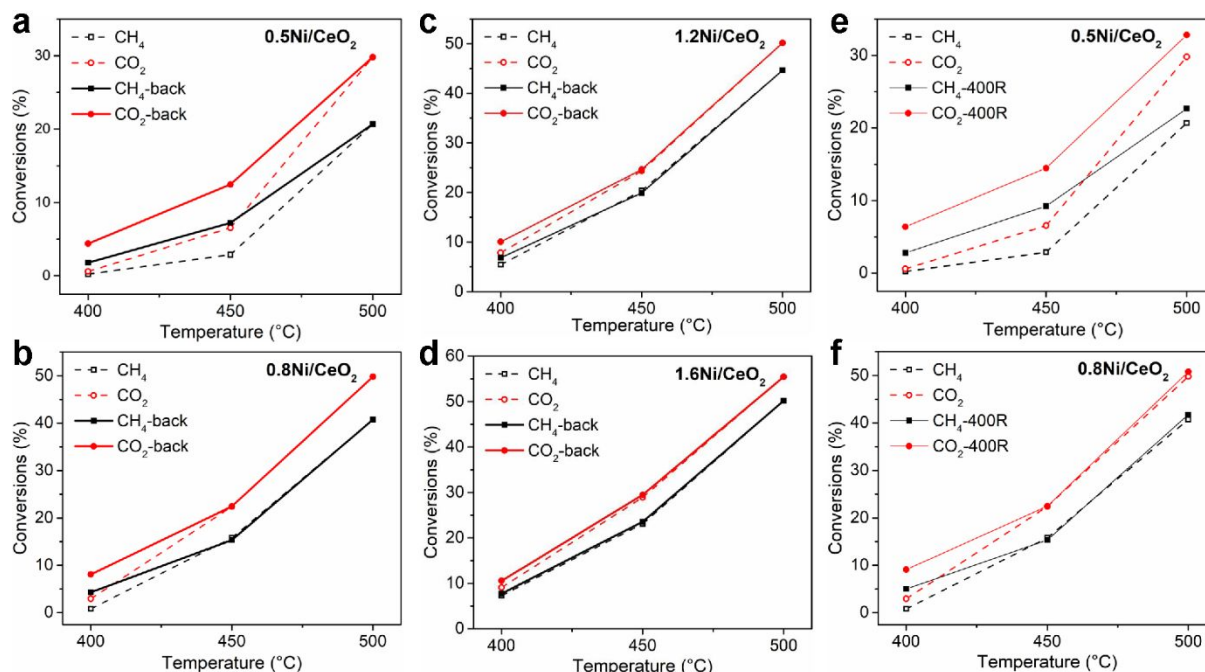
ARTICLE

Fig. 5. DRM catalytic performance comparisons of Ni/CeO$_2$ catalysts with different Ni species. The CH$_4$ & CO$_2$ conversions comparison during ramping and cooling evaluation for (a) 0.5Ni/CeO$_2$, (b) 0.8Ni/CeO$_2$, (c) 1.2Ni/CeO$_2$ and (d) 1.6Ni/CeO$_2$. The CH$_4$ & CO$_2$ conversions comparison with and without pre-reduction before DRM reaction for (e) 0.5Ni/CeO$_2$ and (f) 0.8Ni/CeO$_2$. "400R" represents a pre-reduction at 400 °C in 10%H$_2$/N$_2$ before DRM reactants flowed in. Reaction conditions: [CH$_4$] = [CO$_2$] = 1%, balanced with N$_2$, contact time: 100,000 mL g$_{cat}^{-1}$ h^{-1}.

loading, while improving the surface density of Ni atoms would benefit the aggregation.

It is worth noting that the dominated oxidative Ni clusters on as-prepared 1.2Ni/CeO$_2$ and 1.6Ni/CeO$_2$ are not the active sites, despite the similar catalytic performance during the ramping and cooling process (Fig. 5c, 5d). For instance, with the 1.6Ni/CeO$_2$ catalyst, we recorded the catalytic activity changes at 400 °C (Fig. S10). There is a significant reactivity difference between the 1st minute and the subsequent period, indicating the status of Ni atoms changes once they come in contact with the DRM reactants. Specifically, the originally oxidative Ni clusters are reduced and aggregate under the DRM reactants, suggesting that these original oxidative clusters are not the active sites for DRM reaction.

Ni species on reaction-spent catalysts

Various characterizations were performed on reaction-spent catalysts to investigate the states of nickel after reaction. The diffraction peak of metallic Ni or NiO species was still absent in XRD patterns (Fig. S11), indicating that the aggregated NPs are still below the detection limit of XRD. Moreover, the signal of

metallic Ni species was still absent in XPS (Fig. 6), with Ni^{2+} as the exclusive species on all the reaction-spent catalysts. This may be because the metallic Ni species was oxidized upon
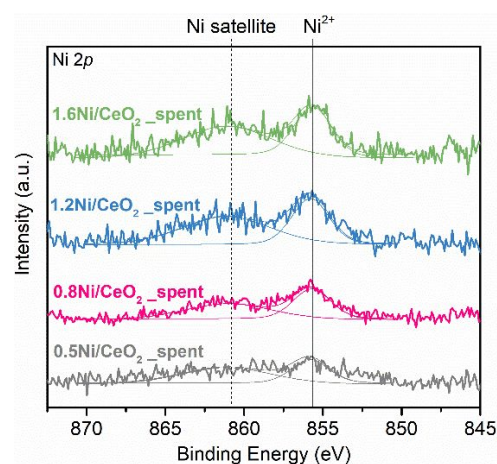

Fig. 6. Ni 2p XPS spectra of reaction-spent Ni/CeO$_2$ samples.

ARTICLE

exposure to air. Despite the similarity of Ce(III) compared with the as-prepared catalysts (Fig. S12a), a great discrepancy in oxygen species was detected after the reaction (Fig. S12b). There are more O-III species at 532.8 eV on the reaction-spent $0.5Ni/CeO_2$ (26.4%, Fig. S12b) attributable to adsorbed water molecules.[29–31] These H_2O molecules were the product of the reverse water gas shift side reaction which employs CO_2 and H_2 to produce CO and H_2O molecules[27,28] and prefers to occur on Ni single atoms.[27] This confirms the presence of some Ni single atoms on the reaction-spent $0.5Ni/CeO_2$, consistent with the H_2/CO results (Fig. S7).

Interestingly, the H_2 TPR profiles with similar reduction peak features indicate that similar Ni NPs or clusters dominate all the spent Ni/CeO_2 catalysts (Fig. S13). More so, we observed some Ni NPs in the size of 5–7 nm even on the reaction-spent $0.5Ni/CeO_2$ by EDS mapping (Fig. 7a), although there are still some highly dispersed Ni species in the visualization field (Fig. 7a, 7b). This verifies that some Ni single atoms aggregated into NPs during the reaction, while others may still be below 2 nm, agreeing with our inference from the low H_2/CO ratio (Fig. S7) and XPS results (Fig. S12b).

Noteworthy, the dispersion of Ni species detected by CO chemisorption was about 50% for all the reaction-spent
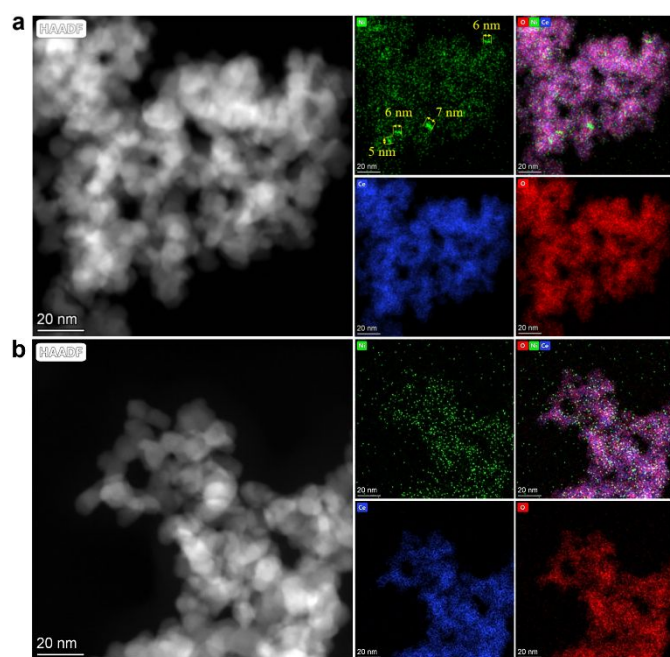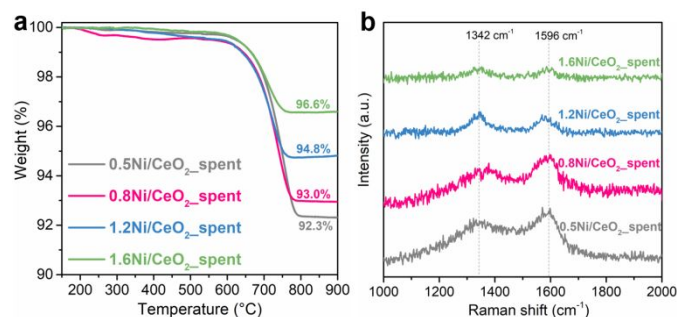

Fig. 8. Carbon deposition characterizations for reaction-spent Ni/CeO_2 catalysts. (a) TG profiles and (b) Raman spectra of reaction-spent catalysts.

samples (Table S2). The calculated average Ni species size would be about 2 nm, according to the correlation between particle size and dispersion (particle diameter (nm) ≈ 1/dispersion (%))[32,33]. This is quite different from what we observed in EDS mapping (Fig. 7). A possible reason is that the deposited carbon covered some surfaces of the Ni NPs, leading to fewer Ni sites available to adsorb CO.

Carbon deposition and elimination

We collected the four reaction-spent catalysts after the DRM elevating test for TG and Raman characterizations to analyze the type and content of deposited carbon (Fig. 8). As displayed in the TG curves (Fig. 8a), the slight weight loss in the temperature range of 200 to 300 °C was due to the oxidation of amorphous carbon,[34,35] while the significant loss ranging from 600 to 800 °C was assigned to the combustion of graphitic carbon.[35,36] In the Raman spectra (Fig. 8b), the peaks centered at 1342 and 1596 cm^{-1} were attributed to sp^3 carbon atoms at disordered sites and sp^2 carbon atoms in graphic rings,[37–39] respectively. Combining the coke signals from TG and Raman characterizations, we found that the content of graphitic carbon increased with the decline of Ni loading amount from $1.6Ni/CeO_2$ to $0.5Ni/CeO_2$.

Given the analyses for Ni species in reaction-spent 0.5 and 1.6 wt.% loaded Ni/CeO_2 samples (see "Ni species on reaction-spent catalysts" section), there are still some Ni single atoms on the reaction-spent $0.5Ni/CeO_2$ sample due to its low Ni density, while NPs dominates on the 1.6 wt.% counterpart owing to its high Ni loading amount. The significant amount of graphitic carbon on the reaction-spent $0.5Ni/CeO_2$ sample suggests that the Ni single atoms may lead to increased carbon deposition or are ineffective at carbon elimination. As we have verified in other Ni catalysts supported by ceria-based materials,[40] the carbon diffusion to be oxidized on smaller Ni species may be

Fig. 7. HAADF-STEM images and EDS mapping of reaction-spent $0.5Ni/CeO_2$ sample. (a) and (b) are two representative observation regions. (a) shows obvious Ni NPs, and (b) displays well-dispersed Ni atoms on the reaction-spent $0.5Ni/CeO_2$ sample.
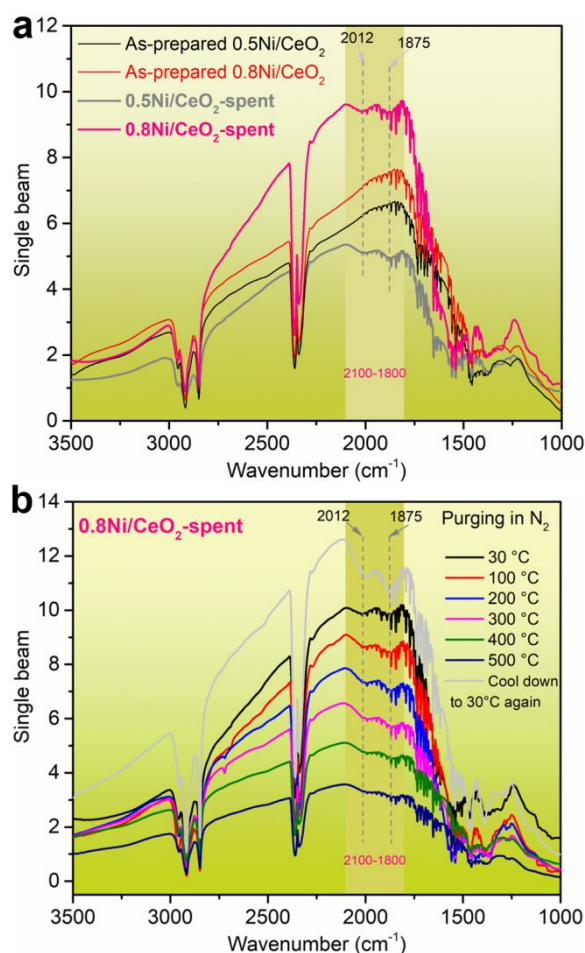
Fig. 9. In situ DRIFTS study for reaction-spent $0.5Ni/CeO_2$ and $0.8Ni/CeO_2$ samples. (a) Background comparison for as-prepared and reaction-spent Ni/CeO_2 catalysts. (b) CO adsorption and coke evolution on $0.8Ni/CeO_2$ during temperature elevating process in N_2.

from ceria,[10,44] it can be deduced that the deposited carbon would diffuse to interface and react with the reactive oxygen during the elevating process. This would result in more Ni atoms being exposed due to the elimination of carbon deposits, and the generated CO can reduce NiO species to metallic states. These two factors result in increased and stronger CO adsorption when cooled down to 30 °C again.

Based on the foregoing, more atomically dispersed Ni atoms on $0.5Ni/CeO_2$ resulted in more carbon deposition during DRM reaction, and it is ineffective for carbon elimination unless aggregated into NPs. The possible reason may be that when the isolated Ni atoms come into contact with DRM reactants at 400 °C, the Ni-O bonds break easily, causing the Ni atoms to migrate and aggregate. The long distance between each Ni atom allows for more CH_4 decomposition, producing more carbon, which eventually covers the Ni sites. In contrast, on samples like $1.6Ni/CeO_2$, more Ni atoms can rapidly aggregate into NPs. The generated carbon on these NPs would diffuse to the interface for oxidation by the surface reactive oxygen. This facilitates the carbon elimination process and therefore decreases the amount of deposited carbon.

Mechanism study

In previously reported DRM reaction mechanism,[45,46] the reaction takes place on ceria-based materials following a bifunctional mechanism: CH_4 would be activated on Me sites to form hydrogen and CH_x intermediates, the surface reactive oxygen converts the CH_x species into CO and hydrogen, and CO_2 adsorbed on the leftover oxygen vacancies of the support to produce CO and fill the vacancy. According to this mechanism, coke formation is suppressed, and the CH_4 is converted into CO

more difficult than that on the larger ones. This would cause a complete coke coverage and deactivation of Ni sites.

The reaction-spent 0.5 and $0.8Ni/CeO_2$ samples with more coke after DRM reaction in a fixed-bed reactor were then characterized by DRIFTS with N_2 purging at room temperature (Fig. 9a). Compared with the as-prepared counterparts, inverted adsorption vibrations centering at 2012 and 1875 cm^{-1} were observed on the reaction-spent samples. Given the fundamentals of DRIFTS measurement,[41] there must be something adsorbing energy in this region of the infrared band. Considering they are reaction-spent samples, the possible adsorbates would be the linear and bridged CO adsorption on 5–15 nm Ni NPs,[42,43] consistent with what we observed from the EDS mapping (Fig. 7). Besides, the deposited carbon is another possible adsorbate. When elevating the chamber temperature with N_2 purging (Fig. 9b), the intensity of the two inverted peaks declined and became less obvious at 500 °C. Interestingly, the inverted peaks reappeared and became stronger when cooled to 30 °C again. If CO is the exclusive adsorbate on Ni species, it must have been desorbed completely at the high temperature of 500 °C and would not reappear upon cooling. Therefore, the deposited carbon contributes to the inverted adsorption peaks. Given the carbon oxidation function of surface reactive oxygen

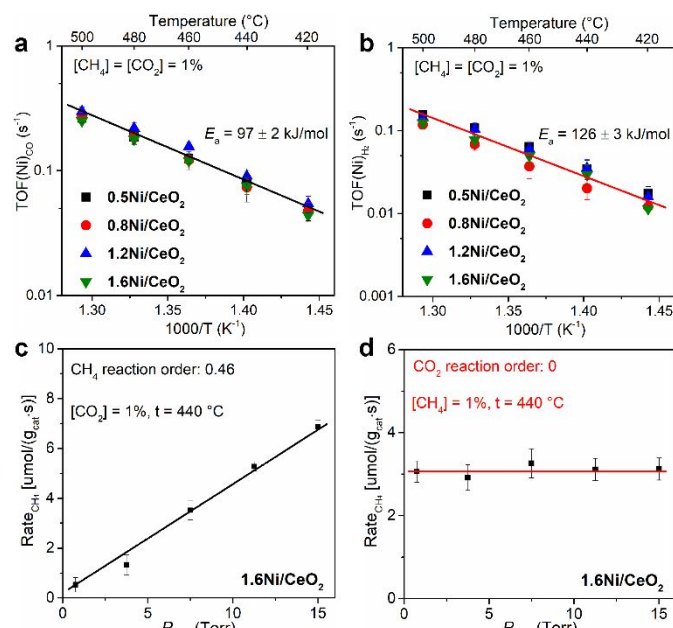**Fig. 10.** Kinetic measurements of different Ni/CeO_2 catalysts. TOF measurements at different temperatures for (a) CO and (b) H_2. Reaction orders with respect to (c) CH_4 and (d) CO_2 at 440 °C. The TOFs were calculated by dividing the overall reaction rate over the exposed Ni atoms measured by CO chemisorption, and the apparent activation energies for CO and H_2 generation were labelled in (a) and (b).

and H$_2$ directly. However, carbon deposits occurred significantly on our ceria supported Ni-based catalysts.

To investigate the reaction mechanism and the discrepancy of Ni species on the four Ni/CeO$_2$ catalysts, we performed kinetic measurements from 420 to 500 °C, ensuring heat and mass transfer issues were avoided. Our turnover frequency (TOF) based on the total Ni loading atoms is similar to the reported DRM catalysts (Table S3). As shown in Fig. 10a and 10b, the four samples exhibited similar activation energy (E_a) values for CO and H$_2$ formation, 97 ± 2 and 126 ± 3 kJ/mol, respectively. These E_a values are highly consistent with other reports.[47] Further, the TOFs based on Ni dispersion are almost identical at the same temperature, i.e., the reaction rates for CO or H$_2$ generation on every exposed Ni atom are identical. This demonstrates that the exposed Ni atoms are the active sites for DRM reaction, and the four Ni/CeO$_2$ catalysts share the same reaction mechanism.

We measured the reaction orders of CH$_4$ and CO$_2$ to further
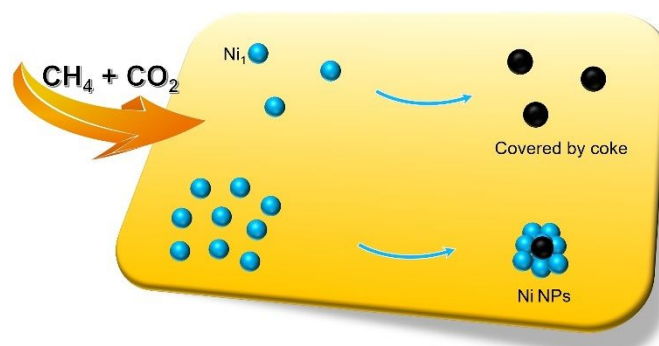

Fig. 12. Schematic for the evolution of atomically dispersed Ni species during DRM reaction.
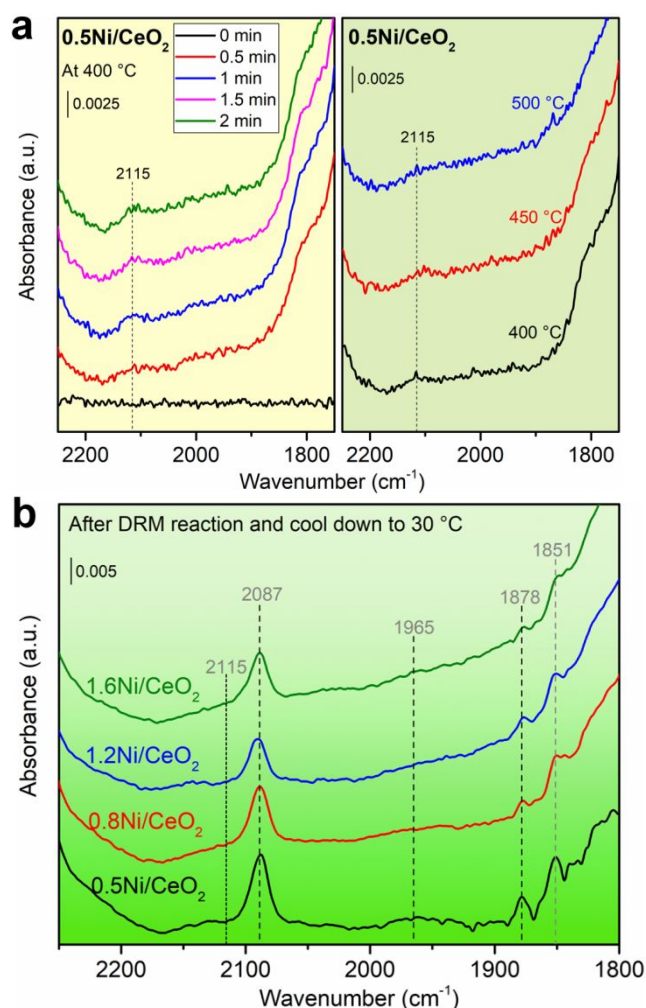

Fig. 11. DRIFTS study under DRM conditions. (a) The initial evolution of Ni species at 400 °C and the changes with temperature elevation. (b) The Ni species comparison of the four Ni/CeO$_2$ catalysts after DRM reaction and cool down to 30 °C. Test conditions: [CH$_4$] = [CO$_2$] = 1%, balanced with N$_2$, elevate from 400 to 500 °C and cool down to 30 °C.

understand the reaction paths (Fig. 10c, 10d). At 440 °C, the reaction orders with respect to CH$_4$ and CO$_2$ are about 0.46 and 0, respectively. This suggests that the reaction rate is dependent on the concentration of CH$_4$, regardless of CO$_2$. The CH$_4$ relevant steps, including CH$_4$ decomposition and carbon elimination, would affect the reaction rate. The resulting carbon deposits detected by TG, Raman, and DRIFTS (Figs. 8, 9) suggest that the elimination of carbon may be the most challenging step for the whole DRM reaction.

To monitor the evolution of Ni species during the reaction, we performed time-resolved DRIFTS experiments on 0.5Ni/CeO$_2$ under DRM conditions. As displayed in Fig. 11a, when the DRM reactants flowed into the sample chamber at 400 °C, a weak CO adsorption vibration centering at 2115 cm^{-1} attributable to CO adsorption on Ni$^+$ atoms[48–50] emerged instantly (0.5 min). We subsequently elevated the temperature from 400 to 500 °C, but did not observe any other CO adsorption vibration except on the Ni$^+$ atoms at 2115 cm^{-1}. Given the observed Ni NPs in the size of 5–7 nm from EDS mapping (Fig. 7), we assigned the vibration mode at 2115 cm^{-1} to CO adsorption on the interfacial Ni$^+$ atoms, i.e., the interface of Ni NPs and ceria support.

When the chamber was cooled down to 30 °C under the mixed DRM reactants and products, the CO adsorption on the four samples were almost identical (Fig. 11b). The vibration mode centering at 2087 cm^{-1} was attributed to linear CO adsorption on 1.1–1.8 nm NPs containing Ni^0 and Ni^{2+} species,[51,52] while the bands at 1965, 1878 and 1851 cm^{-1} were attributable to bridged CO adsorption on Ni^0 NPs.[15,52,53] The discrepancy in Ni species size with that in Fig. 9 was resulted from the difference in sample packing and reactants flow mode between the fixed-bed reactor and DRIFTS.

Why the vibration peaks at room temperature cannot be observed from 400 to 500 °C during DRM reaction (Fig. 11)? This may be because the CO adsorption on Ni atoms is quite weak and prone to desorb at high temperatures.[17] We can observe CO adsorption on interfacial Ni$^+$ atoms (2115 cm^{-1}) because the newly generated CO molecule needs to desorb from these Ni$^+$ atoms. That is, the deposited carbon would diffuse to the interfacial Ni$^+$ atoms and react with the interfacial reactive oxygen to produce CO molecules. Alternatively, the CO$_2$

molecule would adsorb on the interfacial Ni^+ and the oxygen vacancy (after the interfacial reactive oxygen is consumed) simultaneously,[54] then produce another CO molecule. Therefore, the newly formed CO molecules keep desorbing at the interfacial Ni^+ atoms. This is why we can only observe the vibration mode at 2115 cm^{-1}, even at high temperatures.

Based on the preceding, the Ni species would aggregate into NPs upon contact with DRM reactants at 400 °C, but the single-atom Ni with low surface density is difficult to aggregate and prone to produce carbon, as displayed in Fig. 12. Kinetics study and time-resolved DRIFTS under DRM reactions demonstrated that the exposed Ni NPs are the active sites to boost the whole reaction. The CH_4 molecules would decompose to carbon and hydrogen on the surface of these NPs,[10,54] the generated carbon diffuses to interfacial reactive oxygen for oxidation, and the leftover oxygen vacancy would be replenished by CO_2. This completes the reaction cycle. However, the difficulty in carbon diffusion on smaller Ni species may impede its further oxidation by the interfacial reactive oxygen, leading to coke accumulation during the reaction.

Conclusions

In this work, we designed a group of Ni species from single atoms to NPs on CeO_2, and the actual states of Ni species were verified by a series of advanced characterizations. Through DRM studies, the characterizations for the reaction-spent Ni species and carbon deposits, elaborate kinetics, and in situ DRIFTS, we demonstrated that the exposed Ni NPs are the active sites for this reaction. The reaction-spent $0.5Ni/CeO_2$, which retained some single-atom Ni species under reaction condition, experienced the most significant graphitic carbon among the four catalysts, indicating that the isolated Ni atoms may be ineffective in carbon elimination during the low-temperature DRM reaction. Our findings would provide new guidance for the coke-resistant catalyst design.

Experimental

Catalyst preparation

The Ni-free CeO_2 support was synthesized by a coprecipitation method.[18] Specifically, $Ce(NO_3)_3$ (99%, Rongruida, China) solution with a specific concentration was instilled into the aqueous ammonia (analytical grade, FUCHEN) under the violent stirring at 30 °C. The molar ratio of Ce/OH was set to be 1:8. The Ce(III) was oxidized into Ce(IV) by the bubbled air flow during precipitation process. Thereafter, the suspension was maintained at 90 °C for 6 hours with continuous stirring. To produce large pores, a certain amount of polyethylene glycol 4000 and glycine were added, followed by spray drying. Finally, the fresh support was obtained by sequential calcination at 300 °C for 2 hours and 500 °C for 3 hours. The BET surface area of ceria was 103 m^2/g.

To obtain the uniform dispersion of Ni atoms, we loaded different amounts of Ni atoms on ceria by a strong electrostatic adsorption method with $Ni(NH_3)_6Cl_2$ as precursor.[55,56] The pH of $Ni(NH_3)_6Cl_2$ solution with different concentrations was tuned by 25 vol% ammonia solution at room temperature, and the final pH was adjusted to be ~10. Subsequently, an appropriate mass of ceria was added into the above $Ni(NH_3)_6Cl_2$ solution, stirring at 70 °C for 3 hours. The resulting adsorbed solids were filtered, washed with deionized water, and dried at 90 °C overnight. The dried samples were calcined at 500 °C for 3 hours again. The actual Ni loading amount was measured by the inductively coupled plasma atomic emission spectroscopy (ICP-AES) as 0.5, 0.8, 1.2, and 1.6 wt.% on ceria. These Ni/CeO_2 samples are therefore designated as "$0.5Ni/CeO_2$, $0.8Ni/CeO_2$, $1.2Ni/CeO_2$ and $1.6Ni/CeO_2$", respectively. The reaction-spent samples after DRM reaction were postfixed with "_spent".

Material characterization

The specific surface area and pore structure were measured on a Micromeritics ASAP 2460 instrument at −196 °C. The specific surface area was calculated by the Brunauer-Emmett-Teller (BET) method at $P/P_0 \leqslant 0.25$, and the pore structure was analyzed by the N_2 adsorption-desorption cycle with Barrett-Joyner-Halenda (BJH) model. There is a pretreatment at 300 °C for 5 hours under vacuum to remove any adsorbates before measurement. The X-ray diffractometer (XRD) patterns were obtained on a Rigaku SmartLab 9KW instrument (Japan), employing Cu K_α radiation (λ = 1.54178 Å) with a power setting of 40 kV and 150 mA. During measurement, all samples were scanned from 15 to 65 ° at the scanning rate of 10 °/min.

The x-ray photoelectron spectroscopy (XPS) was performed on Thermo ESCALAB 250XI (Mervel Technology). The dominant C1s peak was calibrated to 284.8 eV for all the tested samples. All obtained spectra were analyzed by XPSPEAK using a Shirley background.

Aberration-corrected high-angle annular dark-field scanning transmission electron microscopy (HAADF-STEM) images of as-prepared Ni/CeO_2 samples were obtained on a Titan Cubed Themis G2 300 instrument equipped with a probe corrector. While HAADF-STEM images of reaction-spent Ni/CeO_2 samples were obtained on Talos F200X. The energy dispersive spectrometer (EDS) element mapping was performed on the same instrument with the corresponding HAADF-STEM images.

The x-ray absorption spectroscopy (XAS) was tested at the 12-BM APS beamline with a 13-channel Ge detector in Argonne National Laboratory. Both the transmission and fluorescence modes at Ni K edge were tested. The x-ray absorption edge energy for Ni K edge was calibrated based on Ni foil. The x-ray absorption near edge structure (XANES) spectra were processed by Athena,[57] and the extended x-ray absorption fine structure (EXAFS) data was analyzed by Artemis.

The H_2 temperature programmed reduction (H_2 TPR) measurements of as-prepared Ni/CeO_2 catalysts were conducted on an Autochem II 2920 equipment with TCD as detector. All the samples were first heated to 500 °C and held for 30 minutes in 5% O_2/N_2 flow to get rid of any possible adsorbates. Subsequently, cool down to room temperature with N_2 purging, and switch to 10% H_2/Ar flow when the temperature is stable. After the TCD signal became steady,

ramping to 900 °C at 10 °C/min and recording the TCD signal at the same time. The specific value of H_2 consumption was quantified by testing a certain amount of CuO standard with known purity. CO chemisorption was conducted on the same equipment, and the detailed procedure follows our previous protocol.[18,58] Typically, 100 mg as-prepared or reaction-spent sample was pretreated in Ar at 500 °C for 30 minutes, followed by a reduction treatment at 400 °C in 10% H_2/Ar for 30 minutes. Subsequently, cool down to room temperature with Ar purging, and passivate Ce(III) sites by CO_2 adsorption. Afterwards, remove the excessive CO_2 molecules, inject 15 pulses of 5% CO into the carrier gas, and record the CO signal by TCD. There was a one-minute delay after every CO pulse injection to blow away any weak CO adsorption (usually physisorption). The ratio of Ni: CO was designed to be 1:1 to calculate the amount of exposed Ni atoms.[35,59,60]

Thermogravimetric (TG) analyses were performed on a NETZSCH 209F3A instrument in 20% O_2/N_2 flow from 30 to 900 °C at 10 °C/min. There was a delay at 150 °C for 30 minutes to get rid of any adsorbed H_2O molecules. Raman spectra were collected on HORIBA EVOLVTION (HORIBA Jobinyvon, France). All samples were excited from 500 to 3000 cm^{-1} by a 532 nm laser and scanned five times consecutively. The exposure time for each scan was 15 seconds.

The CO adsorption, in-situ characterizations of carbon elimination, and time-resolved DRM reaction by diffuse reflectance infrared Fourier-transform spectroscopy (DRIFTS) were conducted on a Nicolet 6700 FTIR instrument. It was equipped with a PIKE sample chamber and MCT/A detector. Every spectrum was collected at the resolution of 4 cm^{-1} on OMNIC software. For CO DRIFTS of as-prepared samples, there was a pretreatment at 500 °C in N_2 for 30 minutes to eliminate any adsorbates, then cool down to 30 °C and collect background. When the background spectrum is steady, flow in 1% CO/N_2 and record the adsorption spectra until stabilization. Pertaining to the in-situ characterizations of the coke on spent catalysts after reaction in the fixed-bed reactor, we packed the spent samples into the chamber and collected the background spectra at room temperature and elevated temperatures. When the collection was finished at 500 °C, the chamber was cooled down to room temperature instantly. For DRM DRIFTS, after the pretreatment at 500 °C, the sample chamber was cooled down to 400 °C in N_2, and the background was collected until the spectrum became stable. Subsequently, the proportional DRM stream ([CH_4] = [CO_2] = 1%, balanced with N_2) flowed in, meanwhile, the spectra evolution was recorded for about 1 hour. Afterwards, the chamber was ramped to 450 and 500 °C to further track the changes of Ni species. Finally, stop all the gas flows and cool down to 30 °C with the spectra recording unceasingly.

Evaluation of catalytic performance

The DRM catalytic performance was tested in a fixed-bed reactor. In a typical activity test, 30 mg sample diluted with ~1 g quartz sand and sustained by quartz wool was placed in the middle of the tubular reactor. A K-type thermal couple was inserted into the center of the mixed sample and quartz sand to monitor the temperature changes in real time. All samples were pretreated at 500 °C for 30 minutes in N_2 to remove any remaining adsorbates. Next, cool down to 400 °C with an N_2 purge. In the meantime, flow the DRM feed stream ([CH_4] = [CO_2] = 1% balanced with N_2) into other gas pipes bypassing the reactor and detect online by a gas chromatography (PANNA, A91 Plus) until stabilization. When the DRM reactant concentration reaches a steady state, it is switched into the reactor, detecting the concentrations of CH_4, CO_2, CO, and H_2 for about 1 hour unceasingly. Afterwards, ramp to 450 and 500 °C with the same treatment. Our gas chromatography is equipped with FID and TCD detectors to improve its detection precision at low reactant concentrations, and there is a CH_4 converter before FID to convert the low-concentration CO and CO_2 gases. The conversions of CH_4 and CO_2 during DRM reaction were calculated by the following equations:

$$X(CH_4) = \frac{([CH_4]_{in} - [CH_4]_{out})}{[CH_4]_{in}} \times 100\%$$

$$X(CO_2) = \frac{([CO_2]_{in} - [CO_2]_{out})}{[CO_2]_{in}} \times 100\%$$

Where [CH_4] and [CO_2] are the respective mole concentrations of CH_4 and CO_2 in the feed stream, "in" and "out" denote the gases flowing in and flowing out of the reactor.

Kinetic measurements were performed on the same set-up using a microreactor. The steady-state reaction rates in the temperature range of 420–500 °C were measured under the kinetic regimes. To avoid the heat and mass transfer effects, we adjusted the contact time from 200,000 to 600,000 mL g_{cat}^{-1} h^{-1} during the measurement. Further, the conversions of CH_4 and CO_2 were both controlled below 20%. Turnover frequencies (TOFs, s^{-1}) of CO and H_2 based on the exposed Ni atoms were calculated according to the following equations:

$$TOF(Ni)_{CO} = \frac{F \times [CO]}{22,400 \times 60 \times m_{cat} \times W_{Ni} \times dispersion/58.7}$$

$$TOF(Ni)_{H_2} = \frac{F \times [H_2]}{22,400 \times 60 \times m_{cat} \times W_{Ni} \times dispersion/58.7}$$

Where F, m_{cat}, and W_{Ni} represent the flow rate (mL/min), the mass of catalyst in kinetic tests, and the loading amount of Ni, respectively.

Conflicts of interest

There are no conflicts to declare.

Acknowledgements

Notes and references

1 B. Qiao, A. Wang, X. Yang, L. F. Allard, Z. Jiang, Y. Cui, J. Liu, J. Li and T. Zhang, *Nat. Chem.*, 2011, **3**, 634–641.

2 X.-F. Yang, A. Wang, B. Qiao, J. Li, J. Liu and T. Zhang, *Acc. Chem. Res.*, 2013, **46**, 1740–1748.

3 A. Wang, J. Li and T. Zhang, *Nat. Rev. Chem.*, 2018, **2**, 65–81.

4 S. K. Kaiser, Z. Chen, D. Faust Akl, S. Mitchell and J. Pérez-Ramírez, *Chem. Rev.*, 2020, **120**, 11703–11809.

5 L. Liu and A. Corma, *Chem. Rev.*, 2018, **118**, 4981–5079.

6 M. C. J. Bradford and M. A. VANNICE, *Catal. Rev.*, 1999, **41**, 1–42.

7 D. Pakhare and J. Spivey, *Chem. Soc. Rev.*, 2014, **43**, 7813–7837.

8 G. P. Van Der Laan and A. a. C. M. Beenackers, *Catal. Rev.*, 1999, **41**, 255–318.

9 Y. Chen, J. Wei, M. S. Duyar, V. V. Ordomsky, A. Y. Khodakov and J. Liu, *Chem. Soc. Rev.*, 2021, **50**, 2337–2366.

10 L. P. Teh, H. D. Setiabudi, S. N. Timmiati, M. A. A. Aziz, N. H. R. Annuar and N. N. Ruslan, *Chem. Eng. Sci.*, 2021, **242**, 116606.

11 S. Das, U. Anjum, K. H. Lim, Q. He, A. S. Hoffman, S. R. Bare, S. M. Kozlov, B. C. Gates and S. Kawi, *Small*, 2023, 2207272.

12 Y. Lyu, J. Jocz, R. Xu, E. Stavitski and C. Sievers, *ACS Catal.*, 2020, **10**, 11235–11252.

13 K. Feng, H. Zhang, J. Gao, J. Xu, Y. Dong, Z. Kang and J. Zhong, *Appl. Phys. Lett.*, 2020, **116**, 191903.

14 J. Finzel, K. M. Sanroman Gutierrez, A. S. Hoffman, J. Resasco, P. Christopher and S. R. Bare, *ACS Catal.*, 2023, **13**, 6462–6473.

15 T. Pu, J. Chen, W. Tu, J. Xu, Y.-F. Han, I. E. Wachs and M. Zhu, *J. Catal.*, 2022, **413**, 821–828.

16 X. Yang, M. Huang, H. Huang, D. Li, Y. Zhan and L. Jiang, *Int. J. Hydrogen Energy*, 2022, **47**, 22442–22453.

17 J. Hulva, M. Meier, R. Bliem, Z. Jakub, F. Kraushofer, M. Schmid, U. Diebold, C. Franchini and G. S. Parkinson, *Science*, 2021, **371**, 375–379.

18 H. Wang, J.-X. Liu, L. F. Allard, S. Lee, J. Liu, H. Li, J. Wang, J. Wang, S. H. Oh, W. Li, M. Flytzani-Stephanopoulos, M. Shen, B. R. Goldsmith and M. Yang, *Nat. Commun.*, 2019, **10**, 3808.

19 A. Trovarelli, *Catal. Rev.*, 1996, **38**, 439–520.

20 I. Lucentini, A. Casanovas and J. Llorca, *Int. J. Hydrogen Energy*, 2019, **44**, 12693–12707.

21 L. R. Winter, E. Gomez, B. Yan, S. Yao and J. G. Chen, *Appl. Catal., B*, 2018, **224**, 442–450.

22 M.-J. Kim, S. Joo Park, K. Duk Kim, W. Kim, S. Chan Nam, K. Seok Go and S. Goo Jeon, *J. Ind. Eng. Chem.*, 2023, **119**, 315–326.

23 Y. H. Lee, J. Y. Ahn, D. D. Nguyen, S. W. Chang, S. S. Kim and S. M. Lee, *RSC Adv.*, 2021, **11**, 17648–17657.

24 J. Resasco, L. DeRita, S. Dai, J. P. Chada, M. Xu, J. Yan, J. Finzel, S. Hanukovich, A. S. Hoffman, G. W. Graham, S. R. Bare, X. Pan and P. Christopher, *J. Am. Chem. Soc.*, 2019, **142**, 169–184.

25 Z. An, P. Yang, D. Duan, J. Li, T. Wan, Y. Kong, S. Caratzoulas, S. Xiang, J. Liu, L. Huang, A. I. Frenkel, Y.-Y. Jiang, R. Long, Z. Li and D. G. Vlachos, *Nat. Commun.*, 2023, **14**, 6666.

26 M. K. Nikoo and N. A. S. Amin, *Fuel Process. Technol.*, 2011, **92**, 678–691.

27 F. Doherty, H. Wang, M. Yang and B. R. Goldsmith, *Catal. Sci. Technol.*, 2020, **10**, 5772–5791.

28 H. Xin, L. Lin, R. Li, D. Li, T. Song, R. Mu, Q. Fu and X. Bao, *J. Am. Chem. Soc.*, 2022, **144**, 4874–4882.

29 Z. Liu, S. D. Senanayake and J. A. Rodriguez, *Appl. Catal., B*, 2016, **197**, 184–197.

30 A. Cárdenas-Arenas, A. Quindimil, A. Davó-Quiñonero, E. Bailón-García, D. Lozano-Castelló, U. De-La-Torre, B. Pereda-Ayo, J. A. González-Marcos, J. R. González-Velasco and A. Bueno-López, *Appl. Catal., B*, 2020, **265**, 118538.

31 F. Liang, Y. Yu, W. Zhou, X. Xu and Z. Zhu, *J. Mater. Chem. A*, 2014, **3**, 634–640.

32 O.-L. Pérez, D. Romeu and M. J. Yacamán, *J. Catal.*, 1983, **79**, 240–241.

33 A. Borodziński and M. Bonarowska, *Langmuir*, 1997, **13**, 5613–5620.

34 M. Li and A. C. van Veen, *Appl. Catal., B*, 2018, **237**, 641–648.

35 Y. Wang, R. Zhang and B. Yan, *J. Catal.*, 2022, **407**, 77–89.

36 K. Y. Kim, J. H. Lee, H. Lee, W. Y. Noh, E. H. Kim, E. C. Ra, S. K. Kim, K. An and J. S. Lee, *ACS Catal.*, 2021, **11**, 11091–11102.

37 S. Li, Y. Fu, W. Kong, B. Pan, C. Yuan, F. Cai, H. Zhu, J. Zhang and Y. Sun, *Appl. Catal., B*, 2020, **277**, 118921.

38 L. Bokobza, J.-L. Bruneel and M. Couzi, *Vib. Spectrosc.*, 2014, **74**, 57–63.

39 K. Cao, M. Gong, J. Yang, J. Cai, S. Chu, Z. Chen, B. Shan and R. Chen, *J. Catal.*, 2019, **373**, 351–360.

40 H. Wang, X. Zhu, A. Adogwa, Y. Shen, M. Yang and T.-B. Lu, *Chem. Eng. J.*, 2024, **493**, 152501.

41 *Infrared Spectroscopy: Fundamentals and applications*, John Wiley & Sons, Ltd, Chichester, UK, 2005.

42 L. Azancot, L. F. Bobadilla, M. A. Centeno and J. A. Odriozola, *Appl. Catal., B*, 2021, **285**, 119822.

43 C. Vogt, J. Kranenborg, M. Monai and B. M. Weckhuysen, *ACS Catal.*, 2020, **10**, 1428–1438.

44 L. Wang and F. Wang, *Energy Fuels*, 2022, **36**, 5594–5621.

45 J. Dou, R. Zhang, X. Hao, Z. Bao, T. Wu, B. Wang and F. Yu, *Appl. Catal., B*, 2019, **254**, 612–623.

46 O. Alioui, M. Badawi, A. Erto, M. A. Amin, V. Tirth, B.-H. Jeon, S. Islam, M. Balsamo, M. Virginie, B. Ernst and Y. Benguerba, *Catal. Rev.*, 2022, 1–53.

47 Y. Kathiraser, U. Oemar, E. T. Saw, Z. Li and S. Kawi, *Chem. Eng. J.*, 2015, **278**, 62–78.

48 A. J. Maia, E. B. Pereira, A. C. Sola, N. Homs, P. R. De La Piscina, B. Louis and M. M. Pereira, *Mol. Catal.*, 2018, **458**, 145–151.

49 M. Lallemand, A. Finiels, F. Fajula and V. Hulea, *J. Phys. Chem. C*, 2009, **113**, 20360–20364.

50 A. I. Serykh and M. D. Amiridis, *J. Phys. Chem. C*, 2007, **111**, 17020–17024.

51 M. Németh, F. Somodi and A. Horváth, *J. Phys. Chem. C*, 2019, **123**, 27509–27518.

52 X. Zhang, P. Yan, B. Zhao and Z. Conrad Zhang, *Catal. Sci. Technol.*, 2021, **11**, 297–311.

53 B. Yan, B. Zhao, S. Kattel, Q. Wu, S. Yao, D. Su and J. G. Chen, *J. Catal.*, 2019, **374**, 60–71.

54 Y. Yoon, H. M. You, H. J. Kim, M. T. Curnan, K. Kim and J. W. Han, *Energy Fuels*, 2022, **36**, 9844–9865.

55 J. Regalbuto, *Catalyst Preparation: Science and Engineering*, CRC Press, 2016.

56 M. Akri, S. Zhao, X. Li, K. Zang, A. F. Lee, M. A. Isaacs, W. Xi, Y. Gangarajula, J. Luo, Y. Ren, Y.-T. Cui, L. Li, Y. Su, X. Pan, W. Wen, Y. Pan, K. Wilson, L. Li, B. Qiao, H. Ishii, Y.-F. Liao, A. Wang, X. Wang and T. Zhang, *Nat. Commun.*, 2019, **10**, 5181.

57 B. Ravel and M. Newville, *J. Synchrotron Radiat.*, 2005, **12**, 537–541.

58 H. Wang, J. Dong, L. F. Allard, S. Lee, S. Oh, J. Wang, W. Li, M. Shen and M. Yang, *Appl. Catal., B*, 2019, **244**, 327–339.

59 M. Wang, Q. Zhang, T. Zhang, Y. Wang, J. Wang, K. Long, Z. Song, X. Liu and P. Ning, *Chem. Eng. J.*, 2017, **313**, 1370–1381.

60 D. Shen, J. Wang, Y. Bai, S. Lyu, Y. Zhang, J. Li, L. Li and G. Wang, *Fuel*, 2023, **339**, 127409.

Data availability statement

- Data for this article, including Figures and Tables are available at https://doi.org/DOI.

- The data supporting this article have been included as part of the Supplementary Information.